









A-type Stellar Abundances: A Corollary to *Herschel* Observations of Debris Disks

Zachary H Draper^{1,2} , Brenda Matthews^{1,2} , Kim Venn¹ , David Lambert³ , Grant Kennedy⁴ , and Tatyana Sitnova⁵ 

¹Physics & Astronomy Department, University of Victoria, 3800 Finnerty Road, Victoria, BC, V8P 5C2, Canada; zhd@uvic.ca

²Herzberg Astronomy and Astrophysics, National Research Council of Canada, 5071 West Saanich Road, Victoria, BC V9E 2E7, Canada

³The University of Texas at Austin, Department of Astronomy, RLM 16.316, Austin, TX 78712, USA

⁴University of Warwick, Department of Physics, Coventry CV4 7AL, UK

⁵Institute of Astronomy RAS, 48 Pyatnitskaya Str., 119017, Moscow, Russia

Received 2017 December 22; revised 2018 February 15; accepted 2018 February 20; published 2018 April 18

Abstract

In order to assess the relationship between metallicity and exoplanetary systems, we compare the abundances of AF-type main-sequence stars with debris disk properties assessed using *Herschel* observations of an unbiased survey of nearby stars. Hot stars are not as commonly observed, given their unique constraints in data reduction, lack of metal lines, and “astrophysical noise” from rotation speed. Here, we address that deficiency using new and archival spectra of 83 AF-type stars. We measure the abundances of a few species in addition to Fe in order to classify the stars with Ap/Am or Lambda Boo signatures. Lambda Boo stars have a chemical signature of solar-abundant volatile species and sub-solar refractory abundances that is hypothesized to be altered by the pollution of volatiles. Overall, we see no correlation between debris disks and metallicity, primarily because the sample size is cut significantly when using only reliable fits to the spectroscopic data. The abundance measured from the Mg II 4481 blend is a useful diagnostic because it can be reliably measured at large $v \cdot \sin(i)$ and is found to be lower around stars with bright debris disks. We find that Lambda Boo stars have brighter debris disks compared to a bias-free sample of AF stars. The trend with disk brightness and Mg abundances suggests pollution effects can be significant and used as a marker for the stability of planetary systems. We explore trends with other species, such as with the C/O ratios, but are significantly limited by the low number of reliable detections.

Key words: circumstellar matter – planet–disk interactions – stars: abundances

1. Introduction

A fundamental parameter to explore in the construction and evolution of exoplanetary environments is metallicity. There is evidence for the early, rapid growth of gas giants in systems with super-solar metallicity, as seen in both radial velocity (Fischer & Valenti 2005) and transit surveys (Buchhave et al. 2014). The metallicity trend for terrestrial mass planets is less apparent, but has its proponents (Zhu et al. 2016). Because debris disks coexist within the circumstellar environment, it would logically follow that metallicity should have some impact on their brightness and evolution. However, when metallicity has been tested against IR-excesses levels, there turns out to be no correlation in solar-type stars (Maldonado et al. 2012). Gáspár et al. (2016) claimed that there is a deficit of debris disks at sub-solar metallicity when the dust mass is accounted for, given the disk’s age and flux. This, however, assumes a steady-state model and ignores the effect of stochastic processes, which can play a role in the evolution of debris disks. Even when considering a variation in metallicity beyond just iron abundance, there is no significant correlation, although there is tentative evidence for the slope of refractory metals versus condensation temperature to be linked to the presence of planets (Maldonado et al. 2015). It is important to look beyond just iron, because within an exoplanetary environment there will be a variation in condensation temperatures. Some elements will be in the gas state, available to be accreted, rather than locked onto dust grains, which can be blown out by radiation pressure. These processes become even more important when the central star has a shallow convection layer, such as in AF-type stars, which allow accretion effects to build on the surface.

Often, abundances versus planetary environment observations are limited to FGK (solar-type) stars. In the case of radial velocity surveys, the number of available lines and narrow widths produces a negative bias toward detecting planets around hot stars, making trends with metallicity hard to measure. The best measurements thus far use evolved giants, which were once main-sequence A-type stars, and infer a similar trend to that seen for FGK stars (Zieliński et al. 2012; Niedzielski et al. 2016). However, chemical evolution of the post-main-sequence giants may have changed the stellar metallicity relative to the natal environment in which the planets formed. Abundances for main-sequence A-type stars are problematic in and of themselves, given various effects on their spectrum including, line blending/broadening, fewer absorption lines, and continuum offsets from Stark-broadened Balmer lines, all by virtue of their temperature, surface gravity, and rotation. Furthermore, their lines can be impacted by NLTE effects, which can result in derived abundances that vary depending on which line is used, by upwards of ~ 1 dex (Takeda 1997).

In this study, we take predominately A-type stars from the DEBRIS *Herschel* Survey and measure their abundances for several species and compare to see if any correlations between chemical abundances and disk properties (e.g., brightness) exist. Some common spectral analysis techniques are poorly suited for hot stars. Equivalent width analysis will often encounter problems with broad, blended metal lines. Data-driven methods would struggle to have an adequate training set to train the analysis, as A-stars are typically ignored due to their unique challenges. Given the unique challenges with reducing hot star spectra, we develop a pipeline to systematically analyze both the stellar parameters and synthesize absorption lines of the entire data set. This greatly enhances the ability to track systematic errors.

In Section 2, we outline the optical spectra used in the abundance analysis and the multiwavelength photometry used to characterize the debris disks. Section 3 discusses the analysis of the spectra and disk properties. A more detailed discussion of methodology used in the spectral pipeline is included in the Appendix. Finally, in Section 4, the spectral abundances are discussed relative to the debris disk observations.

2. Data

The initial sample of stars in the survey was selected from the A- to F-type stars in the DEBRIS survey (Thureau et al. 2014, Foreman-Mackey et al. 2013). The motivation of this selection was to sample the A0-F3 spectral range for which the Lambda Boo phenomenon is observed (Paunzen 2004). We extended the spectral range a bit farther into the F-type regime to allow for more survey overlap with previous studies, for verification of data reduction practices. The DEBRIS Survey only targeted main-sequence stars based on their proximity to the zero age main-sequence (ZAMS) in order to exclude giants (Phillips et al. 2010). The age estimates for these stars are distributed fairly evenly between 10 Myr and 1 Gyr (Vican 2012). A summary of the 83 stellar spectra compiled for this study can be seen in Table 1.

2.1. McDonald

Stars within the sample that are in the northern hemisphere were observed over three nights at the McDonald Observatory. The 2.7 meter Harlan J. Smith telescope, with its Robert G. Tull Coudé 2D cross-dispersed echelle spectrograph, was used to obtain $R \sim 60,000$ spectra from 3800–9000 Å (Tull et al. 1995). Basic CCD data reduction techniques were followed using standard IRAF practices for an echelle spectrograph. This process was automated using PyRAF⁶ to subtract dark frames, divide by flats, and extract flux from each echelle order. Wavelength calibration used ThAr lamps, which were identified against a reference ThAr lamp spectrum using a python GUI (see the appendices for more details).

2.2. ESO Archive

Spectra for stars in the southern hemisphere were collected from the ESO archive. Various facilities and instruments were used, such as UVES (Dekker et al. 2000), FEROS (Kaufer et al. 1999), and HARPS (Mayor et al. 2003). These data are already processed into flux-normalized and wavelength-calibrated phase 3 products. UVES data, which were in separate wavelength channels, are combined into continuous 1D spectra to be consistent with the other data products. The pipeline was designed to minimize human intervention and handle 1D spectra independent of the instrument used.

2.3. DEBRIS Survey

In order to categorically identify stars with and without debris disk detections in an unbiased way, we utilized the DEBRIS survey conducted with the *Herschel Space Observatory*. The survey used PACS 100 and 160 μm observations, ideal for detecting debris disks in the temperature range of cold Kuiper Belt analogs (Wyatt 2008). The DEBRIS sample is volume-limited and therefore unbiased in disk brightness or [Fe/H] (Phillips

et al. 2010). We therefore constrain the spectral comparison to this ideal subset of hot stars from 6700 to 10,000 K to assess the correlation of debris disks to stellar metallicity. The stellar temperature cut in the sample was based on stellar effective temperature SED fits to broadband photometry short of 10 μm .

3. Analysis

Throughout this study we tested and experimented with systematic choices in the data reduction. All of the steps described here were implemented into a series of custom Python routines. This provided the framework for using other specialized programs such as MOOG (Snedden 1973) and Balmer9 (Kurucz 1993; Sbordone et al. 2004) to solve for specific solutions. Furthermore, these routines automated reduction into a pipeline to test the entire sample quickly and efficiently so as to determine the best ways to systematically approach the data reduction rather than a specialized reduction of every target.⁷

3.1. Fundamental Stellar Parameters

In order to derive spectral abundances, we first sought to constrain the stellar effective temperature and $\log(g)$. To do this, several techniques were employed (see Figure 1). Given our spectral range of predominantly hot A-type stars, we choose to use the Balmer line profiles and match derived abundances of ionization species (Fe I = Fe II, Mg I = Mg II). For this analysis, we used a broad range of Kurucz ATLAS9 models over the expected range from 5000 K to 12,000 K and 5 to 0 $\log(g)$ (Kurucz 1993). The grid size was in steps of 250 K and 0.5 $\log(g)$, which is sufficient to achieve 0.1 dex precision for the abundances, given the errors in those stellar parameters alone (See Section 3.2). The final adopted stellar parameters in this study are given in Table 2.

3.1.1. Balmer Lines

The Balmer lines are sensitive to both surface gravity and temperature in AF-type stars. They are often strongly Stark-broadened due to an electric field from nearby free electrons and protons on the surface of these hot stars. With proper modeling, the profile along the broadened wings of the line can be a sensitive diagnostic of the stellar parameters. Balmer9 computed the Balmer line profiles for H β , H δ , and H γ (See Figure 2). Each spectrum had hydrogen lines selected and then shifted in wavelength to rest frequencies through a process of binning and minimum finding. This was essential in terms of batch-processing the spectral data in order to correct for any residual radial velocity corrections from the Earth's motion or CCD data reduction. A residual matrix was created by taking the sum of residuals between the models and data. The inverse was taken to make larger values mean higher correlation and then normalized by the maximum value. The wings of the profile were specifically selected by excluding the core of the line around 1 Å to either side of the line center. An example of this residual matrix can be seen in the top left panel of Figure 1.

3.1.2. Ionization Abundance Matching

Another diagnostic that is sensitive to effective temperature and surface gravity is the balance between abundances derived from species in different ionization states. Here, we used Fe

⁶ PyRAF is a product of the Space Telescope Science Institute, which is operated by AURA for NASA.

⁷ The code used in our analysis of this data is available at <http://github.com/zackdraper/HotSAP/>.

Table 1
Summary of the Spectroscopic Data Used in This Study

HD	HR	Instrument	Obs. Date	Archive Filename
HD 110411	HR 4828	FEROS	2009 Jun 04	ADP.2016-09-23T09:05:28.563
HD 16555	HR 778	FEROS	2008 Nov 13	ADP.2016-09-23T06:51:13.288
HD 16970	HR 804	FEROS	2004 Nov 23	ADP.2016-09-21T06:44:02.167
HD 19107	HR 925	FEROS	2008 Nov 13	ADP.2016-09-23T06:51:13.298
HD 197157	HR 7920	FEROS	2015 Jul 06	ADP.2016-09-28T06:54:53.157
HD 210418	HR 8450	FEROS	2009 Jun 03	ADP.2016-09-23T09:05:28.479
HD 222345	HR 8968	FEROS	2008 Nov 12	ADP.2016-09-23T06:51:12.945
HD 222603	HR 8984	FEROS	2008 Nov 12	ADP.2016-09-23T06:51:12.955
HD 223352	HR 9016	FEROS	2009 Jun 03	ADP.2016-09-23T09:05:28.491
HD 2262	HR 100	FEROS	2015 Jul 01	ADP.2016-09-28T06:54:52.364
HD 105452	HR 4623	UVES	2006 Jan 16	ADP.2013-09-26T16:43:43.707
...	2006 Jan 16	ADP.2013-09-26T16:43:43.727
...	2004 Mar 26	ADP.2013-09-26T05:20:08.217
...	2006 Jan 16	ADP.2013-09-26T16:43:43.660
HD 109536	HR 4794	HARPS	2009 Apr 21	ADP.2014-09-23T11:05:00.440
HD 109787	HR 4802	UVES	2011 May 21	ADP.2013-09-28T04:42:26.883
...	2011 May 21	ADP.2013-09-28T04:42:26.243
HD 11171	HR 531	UVES	2001 Nov 22	ADP.2013-09-25T06:07:14.723
...	2001 Nov 22	ADP.2013-09-25T06:07:14.770
...	2001 Nov 22	ADP.2013-09-25T06:07:15.037
...	2001 Nov 22	ADP.2013-09-25T06:07:14.823
HD 118098	HR 5107	HARPS	2006 May 25	ADP.2014-09-16T11:04:46.913
HD 119756	HR 5168	UVES	2004 Mar 25	ADP.2013-09-26T05:18:23.410
...	2004 Mar 25	ADP.2013-09-26T05:18:23.370
HD 120136	HR 5185	UVES	2004 Apr 01	ADP.2013-09-26T05:32:21.853
...	2004 Mar 29	ADP.2013-09-26T05:27:02.840
HD 130109	HR 5511	FEROS	2012 May 20	ADP.2016-09-27T07:02:46.276
HD 15008	HR 705	HARPS	2004 Sep 30	ADP.2014-10-01T10:23:01.147
HD 172555	HR 7012	FEROS	2016 Mar 29	ADP.2016-09-28T11:26:16.365
HD 187642	HR 7557	UVES	2002 Sep 30	ADP.2013-09-25T19:04:50.557
...	2002 Sep 30	ADP.2013-09-25T19:04:50.523
...	2002 Sep 30	ADP.2013-09-25T19:04:51.287
HD 188228	HR 7590	FEROS	2016 Mar 28	ADP.2016-09-28T11:26:17.546
HD 18978	HR 919	HARPS		
HD 202730	HR 8140	HARPS	2006 May 19	ADP.2014-09-16T11:04:29.547
HD 210049	HR 8431	UVES	2009 Sep 17	ADP.2013-09-27T21:14:15.353
...	2009 Sep 17	ADP.2013-09-27T21:14:15.293
...	2010 Jun 16	ADP.2013-09-28T00:10:00.877
HD 212728	HR 8547	HARPS	2007 Dec 06	ADP.2014-09-17T11:22:12.560
HD 213398	HR 8576	HARPS	2007 Dec 06	ADP.2014-09-17T11:24:46.150
HD 215789	HR 8675	UVES	2009 Aug 17	ADP.2013-12-06T16:44:36.067
HD 29875	HR 1502	HARPS	2004 Sep 30	ADP.2014-10-01T10:19:08.070
HD 55892	HR 2740	UVES	2001 Nov 21	ADP.2013-09-25T06:02:47.413
...	2001 Nov 21	ADP.2013-09-25T06:02:47.380
...	2001 Nov 21	ADP.2013-09-25T06:02:47.553
...	2001 Nov 21	ADP.2013-09-25T06:02:47.327
HD 71155	HR 3314	HARPS	2007 Jan 01	ADP.2014-09-17T11:22:52.083
HD 88955	HR 4023	HARPS	2006 Feb 09	ADP.2014-09-16T11:04:44.387
HD 99211	HR 4405	HARPS	2006 Feb 13	ADP.2014-09-16T11:06:20.390
HD 137898	HR 5746	FEROS	2010 Mar 01	ADP.2016-09-23T12:25:53.302
HD 110379	...	UVES	2011 Apr 08	ADP.2013-09-28T04:09:42.250
...	2011 Apr 0	ADP.2013-09-28T04:09:42.300
...	2011 Apr 0	ADP.2013-09-28T04:09:42.287
...	2011 Apr 0	ADP.2013-09-28T04:09:42.277
HD 115892	HR 5028	FEROS	2005 May 27	ADP.2016-09-21T08:16:13.629
HD 56537	HR 2763	McD. Tull	2014 Apr 24	N/A
HD 58946	HR 2852	McD. Tull	2014 Apr 22	N/A
HD 60178	HR 2890	McD. Tull	2014 Apr 22	N/A
HD 60179	HR 2891	McD. Tull	2014 Apr 22	N/A
HD 76644	HR 3569	McD. Tull	2014 Apr 23	N/A
HD 78209	HR 3619	McD. Tull	2014 Apr 22	N/A
HD 79439	HR 3662	McD. Tull	2014 Apr 22	N/A
HD 80081	HR 3690	McD. Tull	2014 Apr 22	N/A
HD 85376	HR 3900	McD. Tull	2014 Apr 22	N/A

Table 1
(Continued)

HD	HR	Instrument	Obs. Date	Archive Filename
HD 87696	HR 3974	McD. Tull	2014 Apr 22	N/A
HD 89021	HR 4033	McD. Tull	2014 Apr 23	N/A
HD 91312	HR 4132	McD. Tull	2014 Apr 23	N/A
HD 95418	HR 4295	McD. Tull	2014 Apr 23	N/A
HD 95608	HR 4300	McD. Tull	2014 Apr 23	N/A
HD 97603	HR 4357	McD. Tull	2014 Apr 24	N/A
HD 102124	HR 4515	McD. Tull	2014 Apr 24	N/A
HD 102647	HR 4534	McD. Tull	2014 Apr 24	N/A
HD 103287	HR 4554	McD. Tull	2014 Apr 23	N/A
HD 104513	HR 4594	McD. Tull	2014 Apr 23	N/A
HD 106591	HR 4660	McD. Tull	2014 Apr 23	N/A
HD 110379	HR 4825	McD. Tull	2014 Apr 24	N/A
HD 110380	HR 4826	McD. Tull	2014 Apr 24	N/A
HD 112412	HR 4914	McD. Tull	2014 Apr 23	N/A
HD 112413	HR 4915	McD. Tull	2014 Apr 23	N/A
HD 116656	HR 5054	McD. Tull	2014 Apr 22	N/A
HD 116657	HR 5055	McD. Tull	2014 Apr 22	N/A
HD 125161	HR 5350	McD. Tull	2014 Apr 22	N/A
HD 125162	HR 5351	McD. Tull	2014 Apr 22	N/A
HD 128167	HR 5447	McD. Tull	2014 Apr 24	N/A
HD 137909	HR 5747	McD. Tull	2014 Apr 24	N/A
HD 139006	HR 5793	McD. Tull	2014 Apr 22	N/A
HD 140436	HR 5849	McD. Tull	2014 Apr 22	N/A
HD 141795	HR 5892	McD. Tull	2014 Apr 22	N/A
HD 156164	HR 6410	McD. Tull	2014 Apr 22	N/A
HD 159541	HR 6554	McD. Tull	2014 Apr 22	N/A
HD 159560	HR 6555	McD. Tull	2014 Apr 22	N/A
HD 165777	HR 6771	McD. Tull	2014 Apr 23	N/A
HD 172167	HR 7001	McD. Tull	2014 Apr 24	N/A
HD 177196	HR 7215	McD. Tull	2014 Apr 22	N/A
HD 180777	HR 7312	McD. Tull	2014 Apr 24	N/A
HD 184006	HR 7420	McD. Tull	2014 Apr 23	N/A
HD 61421	HR 2943	UVES	2002 Feb 27	ADP.2013-09-25T11:23:49.730
...	2002 Feb 27	ADP.2013-09-25T11:23:50.063
...	2002 Feb 27	ADP.2013-09-25T11:23:49.750

Note. The data were taken either from a PI program at McDonald Observatory using the 2D Robert G. Tull Coudé Spectrograph or from archival European Southern Observatory spectra at several telescopes. ARCFIELD keyword names for the ESO data have been listed.

and Mg lines because they have the greatest number of lines for single-ionized and double-ionized species. A small line list was used that had lines with high to moderate equivalent widths, and that were often in isolation from other lines (see Appendix D). Each line was found and fit with a Gaussian profile to identify the line. The equivalent width was measured from the data and passed into MOOG *abfind* in order to compute the abundances. Every model in our range of parameters was then used to derive abundance values for each ionization state. A residual matrix was made using the inverse square of the differences, such that small differences in the derived abundances were highly correlated to the input model. The matrix was again normalized by its maximum value to ensure that the matched ionization abundance would have an equal weight as the Balmer line method. An example of a residual matrix from this method with data from Vega can be seen in the top right panel of Figure 1.

3.1.3. Photometric Methods

Combining the two previous diagnostics would often leave A-type stars still marginally uncertain (see Figure 1,

bottom left), therefore we investigated photometric methods to determine the effective temperature and in turn the corresponding surface gravity. When spectra are continuum-normalized, the relative flux per wavelength is lost, therefore using a photometric technique offers ancillary information to the previous methods.

One way to constrain the effective temperature is to fit a broad UV-to-mid-IR model SED with archival photometry for each of the stars. (see Section 3.6). This method was also compared with the Strömgren method whereby narrowband photometry is compared against synthetic photometry of models to derive effective temperature and $\log(g)$ (Moon & Dworetzky 1985; Napiwotzki et al. 1993). The most degenerate parameter remaining after the two previous methods are applied is surface temperature, which is simply derived from the (b-y) color. It was found that there is a 1σ dispersion offset between the Strömgren and SED effective temperature of ~ 150 K (see Appendix C). The offset appears to have an effect on A-type stars and not F-type stars, with a transition around 7000 K. The Strömgren method was selected over the SED method for two reasons. First, the Strömgren photometry more closely matched

Table 2
Derived Spectroscopic Stellar Parameters for Stars in This Survey

HD	HR	Temperature	log(<i>g</i>)	<i>v</i> ·sin(<i>i</i>)	Am/Ap	Lambda Boo	SB
HD 110411	HR 4828	8812	4.2	160	...	member	...
HD 16555	HR 778	8449	4.6
HD 16970	HR 804	8603	4.1	166
HD 19107	HR 925	8217	4.1	166
HD 197157	HR 7920	8326	4.4	91	doubtful nature
HD 210418	HR 8450	9008	4.2	146	...	non-member	...
HD 222345	HR 8968	8326	4.4	75
HD 222603	HR 8984	8217	4.1	49
HD 223352	HR 9016	9345	4.4	300	...	probable	...
HD 2262	HR 100	8217	4.1	198
HD 105452	HR 4623	7209	2.9	29
HD 109536	HR 4794	7905	3.8	80	doubtful nature
HD 109787	HR 4802	8900	4.2	197
HD 11171	HR 531	7215	2.9	65
HD 118098	HR 5107	8468	4.1	150
HD 119756	HR 5168	6914	2.9
HD 120136	HR 5185	6466	2.4
HD 130109	HR 5511	9008	4.2	300	doubtful nature
HD 15008	HR 705	9078	4.4	172
HD 172555	HR 7012	8094	4.1	115
HD 187642	HR 7557	5000	0.0
HD 188228	HR 7590	9393	4.5	92
HD 18978	HR 919	8440	4.1	124	doubtful nature
HD 202730	HR 8140	8305	4.1	104	misidentified
HD 210049	HR 8431	9147	3.5
HD 212728	HR 8547	7942	3.8	220
HD 213398	HR 8576	9599	4.3	180
HD 215789	HR 8675	5000	0.0
HD 29875	HR 1502	7198	3.4	56	doubtful nature
HD 32297	...	8194	4.6	84
HD 55892	HR 2740	5000	0.0	...	misidentified
HD 71155	HR 3314	9537	4.3	144
HD 88955	HR 4023	9098	4.3	90
HD 99211	HR 4405	7986	3.9	127
HD 137898	HR 5746	8326	4.4	112
HD 110379J	...	7504	3.1	25	doubtful nature
HD 115892	HR 5028	9160	4.3	79
HD 56537	HR 2763	8680	4.1	161
HD 58946	HR 2852	7163	2.8	72	doubtful nature
HD 60178	HR 2890	9157	5.0	22
HD 60179	HR 2891	9473	4.9	17	binary
HD 76644	HR 3569	8242	3.7	138
HD 78209	HR 3619	7733	3.5	40
HD 79439	HR 3662	8155	4.0	174	doubtful nature
HD 80081	HR 3690	8629	4.2	382	...	non-member	...
HD 85376	HR 3900	7741	3.8	110
HD 87696	HR 3974	8198	4.0	129	...	non-member	...
HD 89021	HR 4033	9082	4.3	51	doubtful nature
HD 91312	HR 4132	7999	4.0	119
HD 95418	HR 4295	9448	4.3	38
HD 95608	HR 4300	9088	4.4	17
HD 97603	HR 4357	8428	4.2	178
HD 102124	HR 4515	8234	4.1	150
HD 102647	HR 4534	8881	4.4	130
HD 103287	HR 4554	9308	4.3	168
HD 104513	HR 4594	7514	3.5	71
HD 106591	HR 4660	8860	4.3	370
HD 110379	HR 4825	7429	3.7	33
HD 110380	HR 4826	7445	3.2	72
HD 112412	HR 4914	7184	3.7	32	doubtful nature
HD 112413	HR 4915	7334	3.1	30	prototype of the Ap variable stars
HD 116656	HR 5054	8526	3.9	...	doubtful nature	...	binary
HD 116657	HR 5055	8482	4.2	53
HD 125161	HR 5350	7990	3.4	132

Table 2
(Continued)

HD	HR	Temperature	log(<i>g</i>)	$v \cdot \sin(i)$	Am/Ap	Lambda Boo	SB
HD 125162	HR 5351	8883	4.4	120	...	member	...
HD 128167	HR 5447	6931	3.7	15	...	non-member	...
HD 137909	HR 5747	8084	3.9	23
HD 139006	HR 5793	9303	4.2	120
HD 140436	HR 5849	8982	4.6	100
HD 141795	HR 5892	8530	3.9	25
HD 156164	HR 6410	8673	4.0	250
HD 159541	HR 6554	7517	3.2	69
HD 159560	HR 6555	7488	3.3	47
HD 165777	HR 6771	8647	4.3	56	doubtful nature
HD 172167	HR 7001	9296	4.4	15	...	probable	...
HD 177196	HR 7215	8194	4.1	125
HD 180777	HR 7312	7544	4.4	55
HD 184006	HR 7420	8385	3.6	250
HD 61421	HR 2943	7008	2.9

Note. Literature classifications have also been listed from Renson & Manfroid (2009; Am/Ap catalog), Murphy et al. (2015; lambda boo catalog), and Pourbaix et al. (2004; spectroscopic binaries catalog).

Vega’s derived temperature, which we adopted as a standard star.⁸ Second, since the Strömngren method is strongly related to the spectral features where the absorption lines are being created in the stellar atmospheres the derived temperature may be more closely related to the effective temperature in the line of sight where abundances are measured.

3.2. Abundances

In order to compute the abundances, a broad line list was used based on the Takeda et al. (2007) atlas of Vega (see Appendix D). Given the broad range of spectral types, lines were included because of their proximity to lines of interest, as they would have more significant absorption at lower temperatures. For example, Mg II 4481 lines can become blended with Fe I 4482 lines at temperatures less than ~ 8500 K while being undetectable at temperatures above ~ 8500 K.

For each line, a sub region spanning 10 \AA was selected. Each region was then synthesized using the MOOG *synth*. In order to compare a model spectrum to an observed spectrum in a reliable way, the data must be precisely calibrated to a flat continuum and shifted to the exact rest wavelength. To ensure both of these criteria are met systematically and reliably across numerous lines and stars, many methods were tested. The best method to flatten the continuum was to use a calculus derivative method to determine which parts of the spectrum are part of an absorption line and which are part of the continuum. To precisely shift the spectrum, a 1D cross-residual is made with a solar abundance model to align the absorption features. More details on the specifics of these methods can be seen in Appendices A and B.

Each line was presorted based on whether or not it had a neighboring line within 4 \AA . In cases where lines were sufficiently isolated, the $v \cdot \sin(i)$ was allowed to vary. This is because the depth of the line will vary with the abundance, while the width of the line will vary predominantly with $v \cdot \sin(i)$;

however, both parameters can be degenerate. In cases where multiple species were blended nearby, $v \cdot \sin(i)$ would become too covariant with the elemental abundances. Therefore, using regions of single-element fits allowed the $v \cdot \sin(i)$ of each star to be measured reliably, to fix $v \cdot \sin(i)$ for blended lines with multiple elements (see Figure 3). In particular, Mg I 5183, Ti II 4468, Ti II 4501, Si II 6347, and Si II 6371 were in isolation from blends and strong enough across the range of stellar temperatures to be trusted to derive $v \cdot \sin(i)$ reliably. Si II 6347 does have a blend with Mg II that can make an abundance measurement difficult, but the line itself appears as one line. Mg II 4481 was also useful for this in the hot constraint in A-type stars, because at those temperatures it does not blend with Fe I 4482. Mg and Fe abundances are then coupled to the same metallicity to improve minimization fitting and measurement of the $v \cdot \sin(i)$. It should also be noted that imposing boundary conditions of 0 to 300 km s^{-1} and -2 to 2 dex in abundances becomes necessary to reduce minimization time and provide realistic fits.

Errors in abundances due to uncertainties in either effective temperature or $\log(g)$ were measured by repeating the spectrum synthesis and fitting with models of the nearest offset in the model grid. These errors were on the order of ~ 0.1 dex (See Table 5) and would be less significant than systematic errors stemming from continuum normalization or wavelength offsets from automation. To represent this in the derived abundances error, the residual sum of squares (RSS) for the synthetic fit was added in quadrature to the error in abundance due to temperature and $\log(g)$. This represents a better estimate of the error and flag lines for which the fitting process were reasonable minimization attempts but would not result in a visually good match to the data. Specific lines were also rejected if their equivalent widths were very small (0.05 \AA) or if the RSS was too large (0.01). In most cases, this results in rejection if the line is too weak due to rapid rotation, an offset wavelength, a blended line, or a combination of those factors. The final compilation of the derived abundances and stellar parameters used in this paper can be seen in Table 5.

3.3. Microturbulence

Microturbulence around AF-type main-sequence stars is known to range from 1 to 5 km s^{-1} . Takeda et al. (2008a)

⁸ Vega’s stellar parameters were adopted from (Castelli & Kurucz 1994) to be $T_{\text{eff}} = 9550 \text{ K}$, $\log(g) = 3.95$. The surface temperature varies by $\sim 2000 \text{ K}$ due to rapid rotation, making a single effective surface temperature problematic, and is rather the temperature along the given line of sight. (Yoon et al. 2010; Monnier et al. 2012).

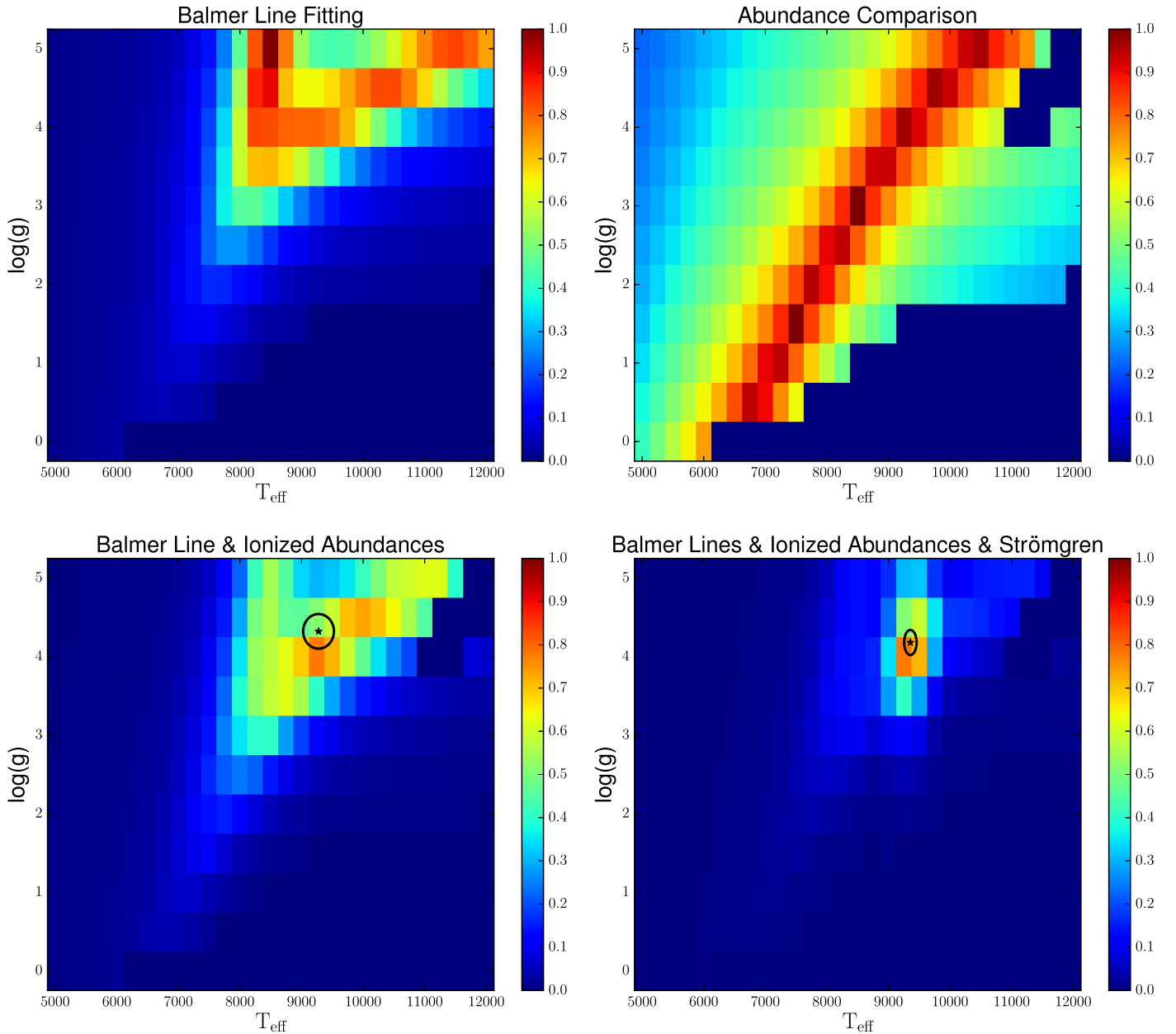


Figure 1. Correlation matrices for models over a range of parameter space, using different diagnostics on the spectrum of Vega. Matrices are normalized by the maximum overall correlation to the data, where blue is a low correlated model near zero and red is a high correlation near 1. On top, Balmer line fitting and matching species of two ionization states (e.g., Fe I = Fe II) are shown. In the bottom left panel, the Balmer line and abundance comparison diagnostics are combined. Given that a broad spread in correlation persists, Strömgen photometry is used to isolate a specific temperature in the bottom right figure.

fit the oxygen lines in 6158 and 7771, but the derived microturbulence from each synthetic line fit would often disagree. Gebran et al. (2014) conducted this analysis again on more slowly rotating A-stars in clusters and found a slightly lower distribution with a peak in average microturbulence of 3 km s^{-1} around $\sim 8000 \text{ K}$. This parameterization of microturbulence would be the only way to diagnose the microturbulence in rapidly rotating AF stars, since the microturbulence and $v \sin(i)$ broadening in each single line profile are degenerate. Even in these measurements the scatter can be on the order of 30%, ranging from $1\text{--}4 \text{ km s}^{-1}$ in a given temperature bin (Gebran et al. 2014). Traditional methods of fitting microturbulence by flattening abundances as a function of equivalent width (because that microturbulence affects stronger lines more readily than weaker lines) is not applicable when the number of lines drops

significantly from rapid rotation. Therefore, the only lines consistently measured are the stronger lines, which can have significant deviations in abundances due to microturbulence. In this study, we set the microturbulence of the Kurucz models at 2 km s^{-1} . If the microturbulence is increased to 4 km s^{-1} , typical Mg II 4481 abundances can change by -0.1 to -0.3 dex. For this line in particular, the abundances will consistently be less than those derived with a lower microturbulence. This is because a change in the line profile will always result in a lower $v \sin(i)$, since a portion of the line broadening is due to the microturbulence, which in turn requires the abundance of the line to drop in order to reduce the core depth of the line. We accept these as a systematic errors that cannot be fit effectively within a single line profile. There is no reason to believe the microturbulence is correlated with debris disk properties, even if

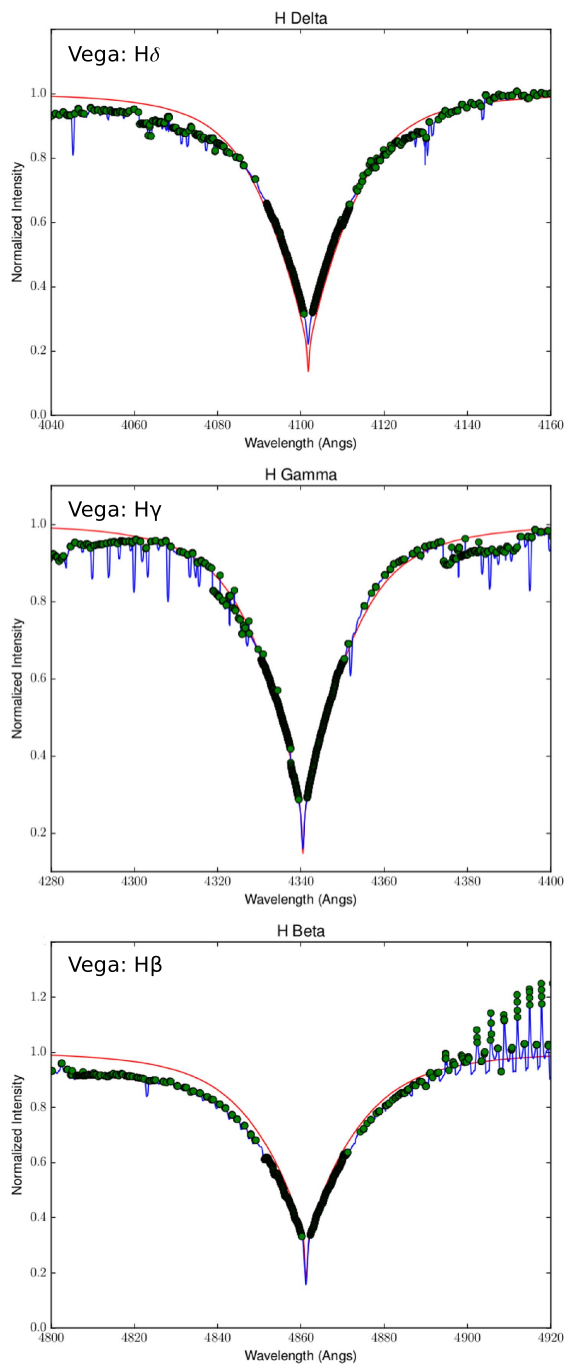


Figure 2. A python wrapper routine was developed to call Balmer9 in order to generate Balmer line models. Above are the Balmer line profiles for Vega, after the best-fit model was selected after the combination of various methods of stellar parameterization. They do not represent the best Balmer line chisqr fit. The data are in blue while the model are in red. The green points are the data points selected for chisqr fitting based on the local derivative and proximity to the line core. A derivative selection isolates the continuum from trace metal lines. The central core 1 Å core of the lines is ignored and the 10 Å to either side of the lines are included. Spurious emission features near H_{β} are unfortunately still selected, but have a lower weight compared to most data points used in the fit. It can also be seen that continuum normalization can still be imperfect and discontinuities exist from merging Echelle orders. This is why using multiple methods can help reduce artifacts from one particular method, in order to seek the most likely model.

a trend with stellar temperature exists across this spectral range, because the disk properties are not correlated with stellar temperature.

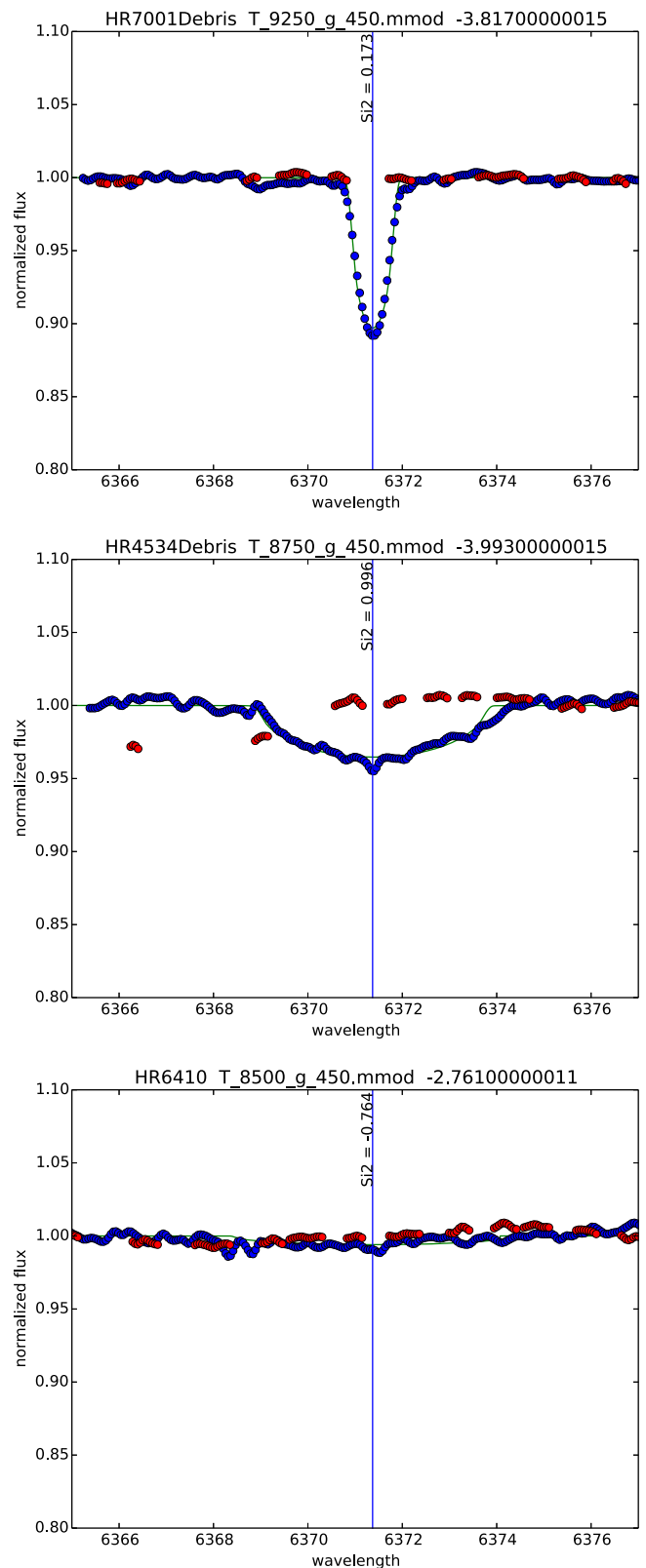


Figure 3. Synthetic model fits to Si 6371 for stars of different $v \sin(i)$. From top to bottom: HR 7001 (Vega) at 22 km s^{-1} , and HR4534 at 111 km s^{-1} , and HR 6410 at what the code determined was 144 km s^{-1} (though this is likely a lower limit). As $v \sin(i)$ approaches 125 km s^{-1} the ability to measure $v \sin(i)$ significantly degrades (and in turn the abundances). The line center is plotted as a vertical line, with the abundance relative to the input model of -0.5 dex displayed. The red dots indicate samples of the original data before continuum and wavelength offsets were measured.

3.4. Limb-darkening

Another effect that can alter the line profile of metal lines is limb-darkening. Stars that rotate rapidly will become non-spherical and have their surface temperature vary dramatically from the pole to the equator. Therefore, the inclination of the system, in tandem with the rotation speed, can alter the line profile and change the derived abundance values. Yoon et al. (2008) and Takeda et al. (2008b) apply non-spherical, limb-darkened models to Vega, after having a known inclination and darkening from resolved near-IR interferometry (Monnier et al. 2012). Takeda et al. (2008b) note that the result for lines that show flattened or “V” profiles is an overestimate of about 0.2 dex. For Mg II 4481, the effect due to rotation versus non-rotational models in Vega amounts to less than 0.1 dex (Yoon et al. 2008). Since the rotation and inclination are not known independently for the entire sample, we accept this as a systematic error in abundances.

3.5. Non-LTE Abundance Corrections

It is important to note that MOOG synthesizes lines under the assumption of local thermodynamic equilibrium (LTE), when in reality these stars’ atmospheres are more complex. We investigate how deviations from LTE affect the abundances relying on the non-LTE calculations from the literature. We take into account deviations from LTE for the lines of the investigated species, where non-LTE abundance corrections⁹ are available in the literature. For an overview of NLTE in A-stars, see Kubát & Korcáková (2004).

3.5.1. Oxygen

The NLTE abundance corrections for oxygen can be very large, depending on the set of lines chosen and have appreciable variations across effective temperature (Takeda 1997; Sitnova et al. 2013). The difference between LTE and non-LTE abundances in oxygen lines increases with higher temperature and lower $\log(g)$ (Sitnova et al. 2013). For our study we use the O I 6158 blend. O 7771 tends to significantly overpredict the derived surface abundances in LTE and require NLTE corrections. We use Takeda (1997), as it has a range of corrections that are valid for our sample of stars. The results for O I 6158 as a function of effective temperature can be seen in Figure 4. Due to the lack of reliable fits in O I 7771 as a broad feature, we utilize O I 6158 in our analysis of oxygen.

3.5.2. Carbon

There are two carbon lines that were found to be of interest in this stellar spectral range, 5052 and 7113 Å. Alexeeva & Mashonkina (2015) and Alexeeva et al. (2016) note that for most G- to A-type main-sequence stars, the NLTE correction is small. For the C I 5052 Å line, the NLTE abundance correction is -0.03 dex for the Sun (Alexeeva & Mashonkina 2015) and -0.04 dex for Vega Alexeeva et al. (2016). The NLTE abundance correction for C I 7113 Å line is -0.06 dex for Vega Alexeeva et al. (2016). Therefore, the corrections are nearly negligible across this spectral range and are not applied to the data.

⁹ The non-LTE abundance correction, $\Delta_{\text{non-LTE}}$, is defined for individual lines as a difference between the non-LTE and LTE abundance.

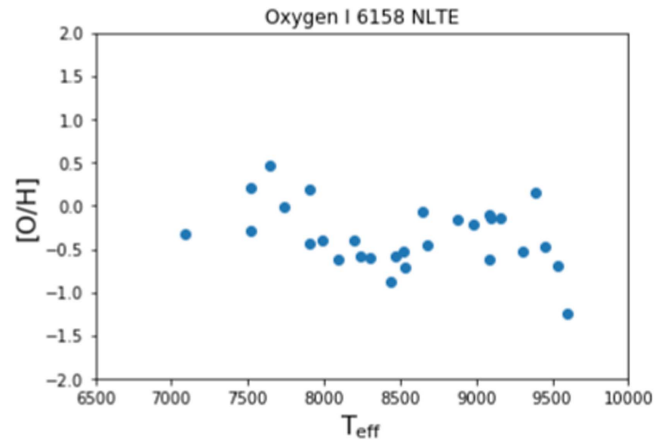


Figure 4. Derived oxygen abundances as a function of effective temperature. In O 6158, the NLTE correction is small relative to NLTE.

3.5.3. Silicon

Wedemeyer (2001) investigated NLTE corrections for silicon, albeit not in the same temperature range. For the Sun, the NLTE correction for Si 6347 Å is -0.1 and for Si 6371 Å is -0.06 . Si 5052 NLTE correction was measured for Vega and was only -0.06 dex. We do not correct any trend across our sample due to NLTE effects, though they appear to be small, on the order of -0.1 dex.

3.6. SED Fitting

In order to measure if a debris disk(s) is present or not, and to what brightness, we utilize *Herschel* PACS photometry that was taken as part of DEBRIS. Photometry at 100 and 160 μm is ideally suited to measure the peak brightness of a cold component of dust typical of a Kuiper Belt analog. Aperture corrections were applied as described in Balog et al. (2014) to *Herschel* photometry. In addition to *Herschel*, archival photometry from optical surveys (Hauck & Mermilliod 1998), *Spitzer* (Su et al. 2006), 2MASS (Cutri et al. 2003), *WISE* (Wright et al. 2010), and *Akari* (Ishihara et al. 2010) were used to construct a multiwavelength SED. From this data, a PHOENIX Ames-COND model was fit to wavelengths less than 10 μm to determine the stellar contribution. A blackbody SED was fit to the longer wavelength photometry if a 3σ IR-excess was found above the expected stellar contribution (e.g., Booth et al. 2013; Kennedy & Wyatt 2014; Draper et al. 2016). We utilize the fractional luminosity of the dust (or lack thereof) to compare with the spectral abundances.

4. Discussion

4.1. Oxygen

After selecting reliable abundance measurements (25/79 stars), we divide the remaining sample into stars of 11/79 with disks and 14/79 without disks. We then compare if there is any distinguishable difference between the two samples that we could infer as being a result of the debris disk’s presence. For oxygen, we take the NLTE of O I 6158 abundances and compare the cumulative distributions with a KS test. As shown in Figure 5, there is no indication that the two samples are from a different underlying population of oxygen abundances. It should also be noted that this is likely a result of the reduced sample size because $v \cdot \sin(i)$ reduces the statistical power of the sample, rather than necessarily a fundamental agreement.

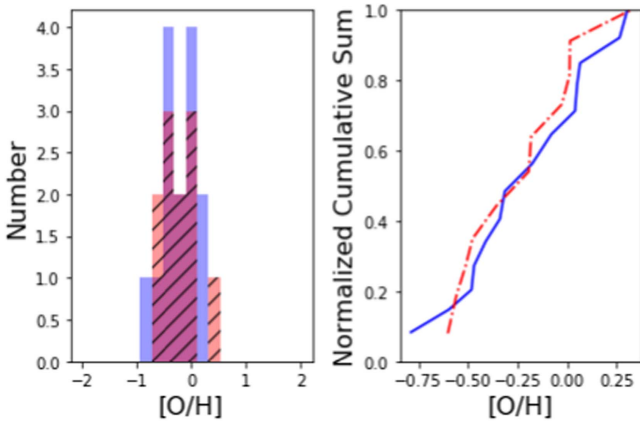


Figure 5. Histograms and cumulative distributions of elemental abundances comparing stars with disks (red, dashed) and stars without disks (blue, solid). Since the number of stars with measured oxygen abundances is a fraction of the total sample (due to poor fitting stemming from “astrophysical” noise of stellar rotation) the variations in the two samples are not statistically significant. Both are consistent with a distribution around solar.

4.2. Lambda Boo Stars

Lambda Boo stars are a type of Population I chemically peculiar star that varies from A0- to F3-type (Paunzen 2004). This is likely due to the fact that the stars are non-convective in their outer envelopes and instead supported by radiation pressure, which allows normally second-order effects to change the surface abundances (Turcotte 2002). The chemical signature of Lambda Boo stars is that species with sublimation temperatures above ~ 1200 K (i.e. refractory) exhibit sub-solar abundances, while species with low sublimation temperatures (i.e., volatile) are solar-abundant (Paunzen 2004; Draper et al. 2016). Several mechanisms have been proposed, but none have been proven beyond a reasonable doubt. One subset of theories is the accretion hypothesis, whereby gas and dust differentiate near the star, such that volatile gas accretes onto the star, while refractory rich dust gets blown out from the system by radiation pressure (Venn & Lambert 1990; Draper et al. 2016). One potential source could be an actively perturbed debris disk that has a high flux of comets near the star (Draper et al. 2016). By polluting the surface with volatiles, the surface refractory abundances drop. The accretion rates needed to sustain a Lambda Boo signature on the central star are much higher than what a kinematically cold debris disk can provide, therefore a dynamic instability from a planet needs to be invoked to perturb the disk (Draper et al. 2016).

Stars in our sample had oxygen abundances that are around solar, so the requirement that they have solar-abundant volatiles was already largely achieved. This is likely a result of the target selection only being stars in the solar neighborhood, in order to be targeted by *Herschel* in DEBRIS. We therefore test if the star has metal-poor refractories in Mg and Si. The contribution of rotational broadening contributes to the “astrophysical” noise in trying to detect a Lambda Boo star. In some cases, its only possible to measure Mg II 4481 because it is one of the strongest metal lines in this spectral range.

If we use Mg II 4481 as a diagnostic for the Lambda Boo classification, (since they are Mg-weak stars), we can obtain a broad measure of the prevalence of the Lambda Boo phenomenon in our sample. While we cannot confirm the solar abundance of volatile elements in all of the stars, we infer for stars that we do measure in the solar neighborhood that

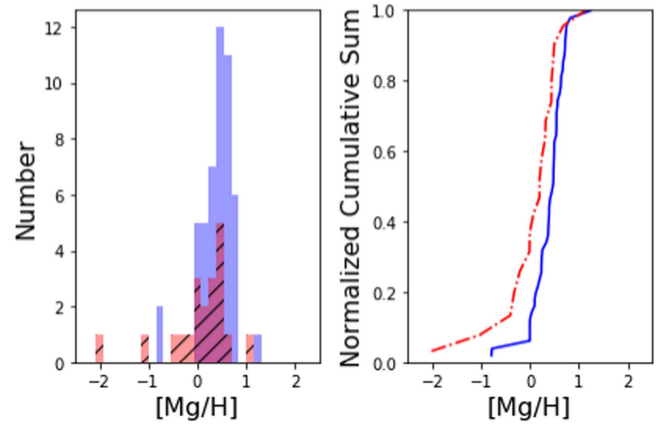


Figure 6. Histogram and cumulative distribution of Mg 4481 measured across the sample. Red denotes stars with a debris disk detected by *Herschel*. Blue denotes stars without any far-IR-excess detected by *Herschel*. There is a tendency (p -value = 0.05 from a 2 sample KS test) for stars with disks to be Mg-weak.

oxygen abundances are roughly solar (see Figure 5). It may therefore be the case that Lambda Boo stars have gone unconfirmed because their rotational broadening prohibits clear classification of volatile elements.

Splitting the sample between stars with and without debris disks detected by *Herschel*, we can see a slight preference for stars to have a lower Mg abundance if they have a debris disk (see Figure 6). From a two-sample KS test, the variation in the cumulative distributions has a low p -value of 0.05. Therefore, it is unlikely that the two samples stem from the same underlying distribution of metallicity at the 2σ level. This suggests the pollution effect is far more prevalent in debris disk systems as a whole, rather than just Lambda Boo stars, which are strongly metal-poor. This implies there could be a gradient of possible accretion and mixing rates related to the Lambda Boo phenomenon (Turcotte 2002).

In the DEBRIS sample there were 100 AF-type hot stars, but only 79 are presented here. In the full sample, there were two previously known Lambda Boo stars (Lambda Boo; HD 125162 and ρ Vir; HD 110411) (Booth et al. 2013). This is approximately consistent with the overall prevalence of Lambda Boo stars, which accounts for $\sim 2\%$ of all field A-stars (Paunzen 2004). There are two other stars that have been identified as probable members, including Vega and HD 223352. All four of these stars have an IR-excess. This in turn would be supportive of potential mechanisms that require a debris disk to cause the accretion of volatile gas out of planetesimals grinding down to create a second-generation gaseous disk (Draper et al. 2016).

In Figure 7, we compare the abundances for stars with a debris disk, as measured by the total fractional luminosity between the disk and star. The fractional luminosity is proportional to both the mass and temperature (and similarly radius) of the disk (Wyatt 2008). The Lambda Boo stars with a Mg metallicity near or below -0.5 dex all have debris disks that are relatively bright at $\text{Log}(F_{\text{IR}}) > -4.8$, compared to other stars observed in the DEBRIS sample with *Herschel*, which have been detected down to $\text{Log}(F_{\text{IR}}) = -5.5$. The outlier at $\text{Log}(F_{\text{IR}}) \sim -3.0$ is HD 172555, which is thought to be a unique case due to a cataclysmic impact of terrestrial-sized objects (Lisse et al. 2009). Therefore, stars with more massive, closer in debris disks, will tend to more likely have a Mg-weak atmosphere, compared to debris disks with farther out, less massive disks. This supports a hypothesis that the pollution effect is due to active perturbations stirring a debris disk, causing an accretion rate of comets that is high enough to cause

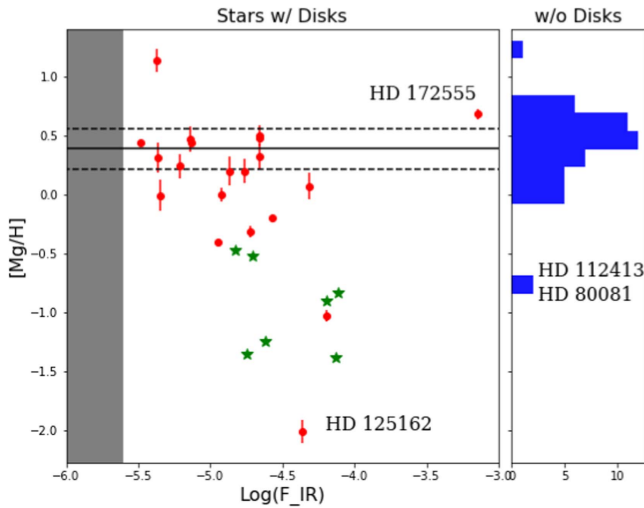


Figure 7. Fractional luminosity as a function of Mg abundance. The red points are stars with a debris disk found in the DEBRIS sample discussed here. The green points are known Lambda Boo stars observed with *Herschel* from Draper et al. (2016). The black line denotes the average Mg abundance of stars without a debris disk from the DEBRIS sample at ~ 0.3 , or slightly above solar. The trend of brighter debris disks having weaker Mg abundance is consistent with the Lambda Boo phenomenon hypothesis of secondary accretion via a stirred debris disk.

the Lambda Boo effect. As a result, not all debris disk stars will have the Lambda Boo signature, but the brightest debris disks, with active planetary scattering, are more likely to have the Lambda Boo signature than their fainter debris disks.

4.2.1. HD 80081 and HD 112413

The only evidence to the contrary from this study are the two stars that have a low Mg abundance but do not have a debris disk. One such star is HD 112413 (HR 4915), which we can verify is an Ap star (high Si abundance, low $v\sin(i)$), and is therefore chemically peculiar for a different reason (Richer et al. 2000; Renson & Manfroid 2009). The other is HD 80081 (HR 3690). This star was once classified as a Lambda Boo star due to the weak Mg 4481 abundance. However, after review of its UV spectrum, it was found to not be metal-weak, as required for a designation of a Lambda Boo star (Paunzen & Gray 1997). It was then downgraded from Lambda Boo status. The only explanation offered so far is that it is a spectroscopic binary, which gives the appearance of a weak Mg line at 4481, but not in the UV where the A-star dominates the flux (Murphy et al. 2015). This could be confirmed with resolved AO spectroscopy from the ground to separate the contribution from either star. In concurrence with fits from Takeda et al. (2008a), the refractory and volatile elements are similarly sub-solar, and therefore not exhibiting a Lambda Boo signature.

4.2.2. HD 223352

HD 223352 is an interesting case study given its Lambda Boo status. The star is a quadruplet of an AB pair with the B component being a binary (Ba and Bb components) and a C component farther out (De Rosa et al. 2011; Phillips 2011). Furthermore, both the A and C component have dust detected with *Herschel*, which makes it one of two unique systems observed thus far to have debris around each individual star in a binary (Rodriguez et al. 2015). The stellocentric distance of the disk around A compared to the projected binary separation of AB leaves the disk around A in an unstable regime, which could lead to a short lifetime as the debris is

dissipated from gravitational perturbations from the binary (Rodriguez et al. 2015). However, in this case a clear mechanism exists—a stellar companion (B) causing the instability—rather than having to invoke an unobserved planet. Therefore, it may be the first system that has a clear causal mechanism for a Lambda Boo phenomenon by an actively perturbed debris disk. The spectra observed for the system would have a combination of A and B components from the spatial separation of $3''5$; however, the B component is ~ 3 orders of magnitude dimmer than the central star (Dommanget & Nys 2002). The membership of this star to the Lambda Boo class is only questionable due to the fact that the high rotation velocity precludes the measurement of volatile elements.

4.3. $v\sin(i)$ versus IR-excess

One trend that stood out was the residual with IR-excess to rotation speed (see Figure 8). Stars with bright debris disks are more likely to be observed around younger stars, as they grind down their planetesimals’ mass with time (Wyatt 2008). Furthermore, older stars will often spin down as they lose angular momentum with age (Skumanich 1972). Therefore, we are likely seeing a gyrochronological effect, such that most of our debris disk stars have $>100 \text{ km s}^{-1}$ rotation speeds. Given that $v\sin(i)$ is a primary source of astrophysical noise in measuring the stellar abundances, this can have an undue effect on the Lambda Boo phenomenon because the sample of stars with debris disks will have a greater likelihood of blended lines with the continuum. It was first noted that Lambda Boo stars tend to have higher rotation speeds than the “normal” A-type stars in Paunzen & Gray (1997). Given that $v\sin(i)$ was used as a selection criteria at one time, it was thought to be a possible bias. However, that trend would be naturally explained by a planet–disk hypothesis, given the gyrochronology.

In terms of the Lambda Boo effect, the rotation speed will dictate the meridional circulation, which controls the timescale for the surface envelope to mix and dissipate any pollution effect. Therefore, young stars that have higher rotation speeds should reduce the Lambda Boo signature instilled early on, as in the case of young Lambda Boo stars observed in the protoplanetary phase (Kama et al. 2015). Older stars observed with the Lambda Boo signature will then need a second-generation gaseous accretion disk, given the timescale is on the order of $\sim 10^6$ years (Turcotte 2002); unless, however, the variation in gas to dust accretion is so strong at birth that the entire surface envelope is depleted of refractory metals. It is unclear how strong or what conditions are necessary to permanently instill the signature at birth. If the effect was not transitional, then it is not clear why Lambda Boo stars seem to all have bright debris disks (Draper et al. 2016). Otherwise, they should have a similar rate of detected debris disks as the general population of A-type stars, 25% (Thureau et al. 2014). A survey of Lambda Boo stars in the far-IR without a bias toward Lambda Boo stars with known IR-excesses is needed to verify the higher prevalence of debris disks around Lambda Boo stars (e.g., Gray et al. 2017).

4.4. Planetesimal Formation Chemistry

Through simulations of planet formation that trace the chemical evolution of planetesimal growth, there is evidence that the range of stellar abundances could change the pathways of grain growth (Carter-Bond et al. 2012). Key ratios can then alter the planet formation process to grow planets significantly different than our own. We therefore would like to also know if these key ratios impact the planetesimal growth for the progenitors of debris disks.

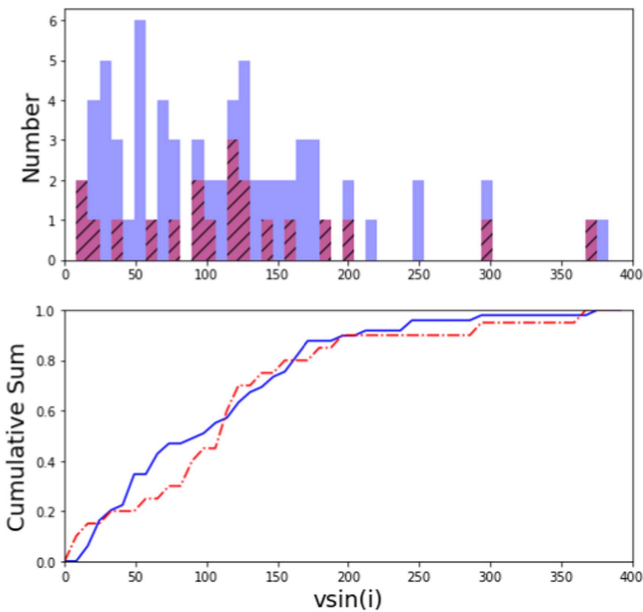


Figure 8. Distribution of $v \sin(i)$ as measured from the Mg II 4481 line. A relative paucity of stars rotating at $\sim 75 \text{ km s}^{-1}$ is likely due to a gyrochronology effect, such that stars with debris disks are often younger, and rotate more rapidly than older stars.

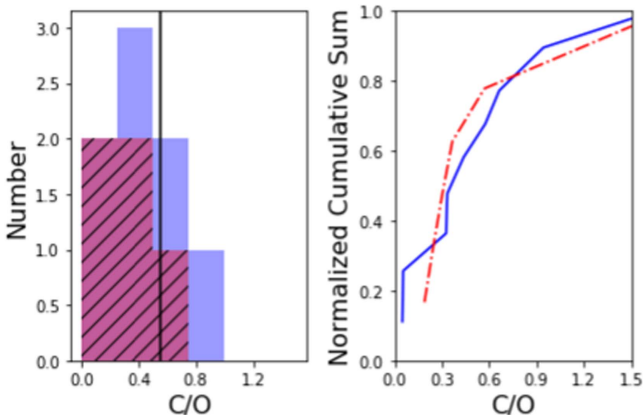


Figure 9. Carbon-to-oxygen ratio for the sub-sample of stars that had a sufficiently good fit to the carbon and oxygen lines. The black line denotes the solar value of C/O. The difference between stars with and without debris disks is not statistically significant, due to low numbers. A general favoring of sub-solar C/O is found, though this would be in the right direction for differential diffusion in slow-rotating A-stars (Am phenomenon; Richer et al. 2000). Their slow rotations also make their C and O abundances easier to measure, introducing a potential bias.

4.4.1. C/O Ratio

The C/O ratio between planets and stars has been found to vary. It is possible that the planetary C/O ratio itself traces where the planet formed in the protoplanetary disk versus where it is currently located. In our sample the quality of the fit to the abundances causes a significant reduction of the sample. Again, this stems mostly from the “astrophysical noise” of stellar rotation making line fitting problematic. In Figure 9, the C/O ratio for stars with and without debris disks can be seen. The measurements rely on C 5052, C 7113, O 6158, and O 7771-5. The smaller sample set means the deviations found are not statistically significant, though there seems to be a preference of sub-solar C/O ratios in the sample stars. Since the bias is for low $v \sin(i)$ stars to have more easily measured

abundances, there may be radiative forces effecting the ratio due to differential diffusion of elements in Ap/Am stars that occur at low rotation speeds. Therefore, the intrinsic C/O ratio would likely be offset to lower carbon and higher oxygen (i.e., lower C/O ratios), potentially by 0.2 dex (Richer et al. 2000).

5. Conclusions

In this study, we measured the metal abundances in stars for which the debris disk properties were known consistently and reliably through far-IR observations from *Herschel*. The main conclusions we draw are the following.

1. Stars with faint debris disks tend to have Mg abundances that are consistent with stars that do not have a debris disk.
2. Stars that are comparatively Mg-weak tend to be around stars with debris disks and those disks are relatively brighter than the typical sample of debris disks seen in this paper.
3. The lack of Lambda Boo stars at low rotation speeds could be explained by the variation in $v \sin(i)$ distributions due to younger stars having faster rotation speeds and therefore more likely having a bright debris disk.
4. HD 80081 can be an interesting case study in the future because it is Mg-weak, but does not have a debris disk to explain a pollution effect.
5. HD 223352 would also be an interesting case study because it is a Lambda Boo candidate with a debris disk that is known to be unstable from a stellar companion and has a solar-type companion to investigate the natal metallicity of the system.

The fundamental data reduction issues for A-type stars were addressed and allowed for systematic analysis of possible errors in a consistent manner. Many other pipelines that perform spectral analysis on large samples are not adequate for handling specific challenges to hot stars. The issues that limited the conclusions of this study were largely astrophysical. Stars with large rotation speeds greater than 125 km s^{-1} did not produce strong enough absorption profiles to measure independently from the continuum, resulting in them being dropped from the sample. Mg 4481 allowed for nearly the whole sample to be studied as a function of metallicity regardless of $v \sin(i)$. Furthermore, A-type stars can have strong NLTE effects that have to be accounted for, but correction tables are not widely available in the literature. The selection of only *Herschel* DEBRIS targets meant most stars were confined to the solar neighborhood, which limited the range of metallicities studied. Unresolved debris disk surveys of stars at greater distances in the far-IR should be considered to reach lower metallicity regions. In the future this type of analysis could be extended to solar-type stars, which will not suffer from the lack of spectroscopic lines, albeit while still being limited by the far-IR observations only being in the solar neighborhood.

With the aim of understanding the Lambda Boo phenomenon, we have searched for more class members in a sample of stars that were systematically searched for debris disks. We did not find any new Lambda Boo stars. Therefore, if the Lambda Boo phenomenon is linked to debris disks, the phenomenon itself is not the explicit result of debris disks. There does, however, tend to be brighter debris disks associated with Lambda Boo stars relative to the unbiased DEBRIS sample. While we cannot suggest that, given the low numbers, all Lambda Boo stars should have debris disks, we find that they

mostly do, both in this broad survey of A-type stars and in a targeted *Herschel* program (Draper et al. 2016).

If the Lambda Boo phenomenon were caused by planetary scattering of a debris disk, it could provide an important constraint on the broad stability of exoplanetary systems. Since there are other scattering mechanisms (i.e., self-stirring, ISM interactions) it may be possible that you can have a bright debris disk around an A-star but not achieve an accretion rate high enough to cause an abundance anomaly. Relatively average levels of $v \cdot \sin(i)$ can erode a detailed abundance analysis; therefore many A-stars are not classifiable. For example, Vega's designation as a Lambda Boo star is assisted by its pole-on viewing geometry. If we only viewed the Mg profile we would only conclude it was partially Mg-weak, while having no constraint on its volatile abundance content, a requirement to make it a "probable" Lambda Boo member given the definitively solar oxygen content. It may be that some of the fast-rotators in this sample are similar to Vega, but lack the volatile element spectral features to reliably classify them. If it can be linked to planetary scattering, than roughly 12.5% of stars with debris disks are undergoing a planetary instability (0.25 fraction of stars with debris disks/0.02 fraction of Lambda Boo stars).

This work is based on data obtained from the ESO Science Archive Facility. Z.H.D. and B.C.M. acknowledge a Discovery Grant and Accelerator Supplement from the Natural Science and Engineering Research Council of Canada. D.L.L. thanks the Robert A. Welch Foundation of Houston, Texas for support through grant F-634. G.M.K. is supported by the Royal Society as a Royal Society University Research Fellow.

Appendix A Continuum Normalization

For steps that required continuum normalization, a general prescription was used to find the continuum points in the spectrum. This could either be at the echelle blaze function extracting from the CCD or in each synthesis window. When normalizing the blaze function, a prescription from Zhao et al. (2006) was used. The general procedure is to normalize to the maximum value that flattens inflection points. Strong lines are identified and ignored as large offsets to record the high point values. The values left over are selected from the unmodified data to then fit a polynomial to normalize the spectra.

In a second iteration, each window of a given line of interest is normalized again to remove any residual continuum offset to more adequately match a synthesized spectrum. Sousa et al. (2007) outlines an effective way to automate this procedure. Effectively, the first and second derivative of every point in the spectrum are taken. This allows the identification of flat regions (the first derivative near zero) and places where the slope is not actively changing (the second derivative near zero). Some tuning has to be done to set a threshold for how close the zero-points should be selected based on the noise level in the data. Smoothing the data was also very effective at improving the solution. Identifying points this way can then allow a polynomial fit to normalize the data before spectrum synthesis occurs.

Appendix B Wavelength Corrections

The spectra are wavelength-calibrated using ThAr lamps to be at the Earth-centric reference frame. Since the abundances are the primary concern, we need to employ a broadly

applicable method to get all the stellar spectrum into the rest-frame with milli-angstrom accuracy to adequately synthesize the spectrum. This is done in successive stages to continually improve the wavelength solution to better accuracy.

First, each spectrum is aggressively median-filtered to smooth the spectrum devoid of lines other than broad Balmer lines. Then, broad search windows of $\sim 100 \text{ \AA}$ can find the minimum value from the rest frequency of Balmer lines. A linear shift can be calculated to conform the unfiltered data and account for the largest shift, which is due to Earth's motion.

In a second iteration, strong metal lines are added as reference points and found as minimum values in narrower search windows of $\sim 10 \text{ \AA}$. This gives broader wavelength reference points across the entire spectrum. At this point, it is beneficial to fit the spectrum with a quadratic, as errors in the wavelength calibration of the instrument could be impactful by a few \AA from one end of the spectrum to the other. By fitting with a quadratic and applying this shift, it is possible to get a fully consistent spectrum, in an automated way, to within a few \AA accuracy.

Finally, in a third iteration, to achieve sub-Angstrom precision applicable for spectrum synthesis, without human intervention, a cross-correlation is used. For each window centered on a line of interest, a synthetic model of solar metallicity, at $25 \text{ km s}^{-1} v \cdot \sin(i)$, is created to use as a reference. Then, the model is shifted with respect to the data, multiplied, and summed to give a vector of correlation with respect to wavelength shift. The continuum-normalized spectrum is inverted above 1, so that when absorption lines match up, the larger the resulting value will be. The shift is allowed to go 3 \AA to match the precision of the previous iteration. In cases where multiple lines are present, or blended, it can be even more accurate, as it can match strong to strong and weak to weak lines at the right separations. Even though the $v \cdot \sin(i)$ of the model reference often will not be accurate, the relative correlation at the core of the lines is still larger and therefore representative of the wavelength shift.

Appendix C Strömgren versus SED Effective Temperatures

In order to determine the spectral effective temperature, we investigated two photometric methods on the entire DEBRIS sample as a consistency check. The Strömgren method uses photometry from (Paunzen 2015) and computes the effective temperature using the prescription from Moon & Dworetzky (1985) implemented in the IDL code *wbybeta.pro*.¹⁰ The SED method compiles photometry from multiple all sky surveys, when data are available (Kennedy et al. 2012), and fits a PHOENIX model atmosphere (Brott & Hauschildt 2005). The surveys utilized include optical-to-mid-IR from Hauck & Mermilliod (1998) and Mermilliod (2006), 2MASS (Cutri et al. 2003), WISE (Wright et al. 2010), *Spitzer* (Su et al. 2006; Chen et al. 2009; Morales et al. 2009), and *Akari* (Ishihara et al. 2010).

We find that there is a systematic trend for stars to be hotter from the Strömgren method than the SED method (see Figure 10). However, this appears to only affect stars greater than 7500 K, which are predominantly the stars of interest in this paper. Stars greater than 7500 K seem to be offset by $\sim 150 \text{ K}$, which also happens to be the FWHM of both populations, giving a 1σ offset between the two temperature ranges.

¹⁰ Source: NASA IDL Code Library.

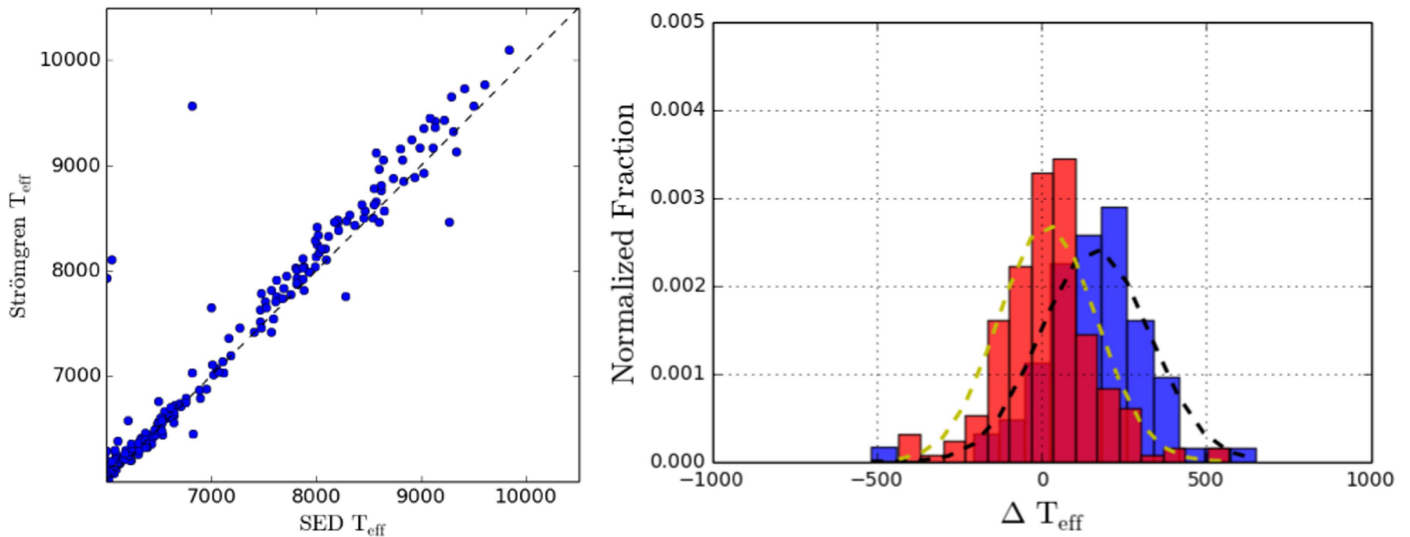


Figure 10. (Left) Scatter plot showing the DEBRIS survey comparing SED temperature to Strömgren temperature. A one-to-one line is overlotted. At about 7500 K, the agreement between the two methods has a marked departure. (Right) Normalized distributions of the difference between the two methods. Gaussians are fit to each distribution and show that the stars greater than 7500 K have a 1σ offset of 150 K vs. the lower temperature stars that are in good agreement.

Appendix D Complete Line Lists and Abundances

In this study, selected lines were taken from the Takeda et al. (2007) atlas of Vega. For reference, the selected line properties that were used in this paper are repeated here (see Table 3). When trying to determine the stellar parameters, a wider list of Mg and Fe is used (See Table 4). For the complete set of data used in the figures of this paper see Table 5.

Table 3
Spectral Line Data Used to Synthetically Fit and Derive Metal Abundances in This Paper (Takeda et al. 2007)

Species	Wavelength (Å)	eV	log(<i>g</i> ^l)
Mg II	4481.126	8.863	0.740
Mg II	4481.150	8.863	-0.560
Mg II	4481.325	8.864	0.590
Fe I	4482.252	2.223	-1.649
Fe I	4482.325	3.654	-1.350
C I	5052.167	7.685	-1.648
Mg I	5183.604	2.717	-0.180
O I	6155.961	10.740	-1.401
O I	6155.971	10.740	-1.051
O I	6155.989	10.740	-1.161
O I	6156.737	10.740	-1.521
O I	6156.755	10.740	-0.931
O I	6156.778	10.740	-0.731
O I	6158.149	10.741	-1.891
O I	6158.172	10.741	-1.031
O I	6158.187	10.741	-0.441
Si II	6347.109	8.121	0.297
Si II	6371.371	8.121	-0.003
C I	7113.178	8.647	-0.350
O I	7771.944	9.146	0.324
O I	7774.166	9.146	0.174
O I	7775.388	9.146	-0.046

Table 4
Spectral Line Data Used to Determine the Stellar Parameters by Matching Abundances between Species in Different Ionization States

Species	Wavelength (Å)	eV	log(<i>g</i> ^l)
Mg I	4702.991	4.346	-0.67
Mg I	5183.604	2.717	-0.18
Mg I	5711.088	4.346	-1.83
Mg I	5528.405	4.346	-0.62
Mg II	4242.448	11.56	-1.07
Mg II	4242.542	11.56	-1.23
Mg II	4427.994	9.995	-1.21
Mg II	4481.126	8.863	0.74
Mg II	4481.150	8.863	-0.56
Mg II	4481.325	8.864	0.59
Fe I	3920.26	0.120	-1.75
Fe I	3997.39	2.730	-0.39
Fe I	4005.25	1.560	-0.61
Fe I	4045.82	1.480	0.28
Fe I	4063.60	1.560	-0.61
Fe I	4071.74	1.610	-0.02
Fe I	4202.03	1.480	-0.71
Fe I	4235.94	2.430	-0.34
Fe I	4260.48	2.400	0.02
Fe I	4282.41	2.180	-0.81
Fe I	4466.55	2.830	-0.59
Fe II	3922.91	7.516	-1.20
Fe II	4233.17	2.580	-2.00
Fe II	4472.92	2.860	-2.21
Fe II	4508.28	2.860	-2.21
Fe II	4515.34	2.840	-2.48
Fe II	4520.23	2.810	-2.60
Fe II	4522.63	2.840	-2.03
Fe II	4541.52	2.860	-3.05
Fe II	4576.33	2.840	-3.04
Fe II	4582.84	2.840	-3.10
Fe II	4583.83	2.810	-2.02
Fe II	4629.34	2.810	-2.37

Note. Only lines that had a reliable fit are used and vary depending on the data/star. (Takeda et al. 2007).

Table 5
Full Table of Derived Stellar Parameters and Abundances Used in This Paper

HD	HR	Temperature	log(<i>g</i>)	<i>v</i> -sin(<i>i</i>)	Mg II 4481	±error	O I 6158	±error	C I 5052	±error	C I 7113	±error
HD 110411	HR 4828	8812	4.2	160	-0.53	0.08
HD 16555	HR 778	8449	4.6
HD 16970	HR 804	8603	4.1	166	0.74	0.05
HD 19107	HR 925	8217	4.1	166	0.74	0.01
HD 197157	HR 7920	8326	4.4	91	1.22	0.08	-0.28	0.01
HD 210418	HR 8450	9008	4.2	146	0.50	0.09
HD 222345	HR 8968	8326	4.4	75	1.22	0.10
HD 222603	HR 8984	8217	4.1	49	0.98	0.06
HD 223352	HR 9016	9345	4.4	300	0.30	0.00
HD 2262	HR 100	8217	4.1	198	0.94	0.04
HD 105452	HR 4623	7209	2.9	29	0.54	0.10
HD 109536	HR 4794	7905	3.8	80	0.95	0.04	0.27	0.02
HD 109787	HR 4802	8900	4.2	197	0.60	0.11
HD 11171	HR 531	7215	2.9	65	1.64	0.14
HD 118098	HR 5107	8468	4.1	150	0.50	0.06	-0.48	0.01
HD 119756	HR 5168	6914	2.9
HD 120136	HR 5185	6466	2.4
HD 130109	HR 5511	9008	4.2	300	0.50	0.10
HD 15008	HR 705	9078	4.4	172	0.76	0.12
HD 172555	HR 7012	8094	4.1	115	1.18	0.07	-0.56	0.03
HD 187642	HR 7557	5000	0
HD 188228	HR 7590	9393	4.5	92	0.81	0.19	0.32	0.03	-0.46	0.03
HD 18978	HR 919	8440	4.1	124	0.62	0.05	-0.79	0.01	-0.31	0.15
HD 202730	HR 8140	8305	4.1	104	0.94	0.03	-0.51	0.06
HD 210049	HR 8431	9147	3.5
HD 212728	HR 8547	7942	3.8	220	1.00	0.00
HD 213398	HR 8576	9599	4.3	180	0.50	0.03	-0.60	0.00
HD 215789	HR 8675	5000	0
HD 29875	HR 1502	7198	3.4	56	1.33	0.13
HD 32297	...	8194	4.6	84	0.39	0.01	-0.31	0.00	-0.55	0.09	-0.28	0.01
HD 55892	HR 2740	5000	0
HD 71155	HR 3314	9537	4.3	144	0.57	0.17	-0.19	0.01	-0.18	0.04
HD 88955	HR 4023	9098	4.3	90	0.74	0.12	0.02	0.03	-0.16	0.04
HD 99211	HR 4405	7986	3.9	127	0.89	0.00	-0.31	0.00	-0.41	0.09
HD 137898	HR 5746	8326	4.4	112	1.21	0.07
HD 110379	...	7504	3.1	25	0.60	0.19
HD 115892	HR 5028	9160	4.3	79	0.97	0.17	0.01	0.03	-0.18	0.05
HD 56537	HR 2763	8680	4.1	161	1.14	0.11	-0.34	0.04
HD 58946	HR 2852	7163	2.8	72	0.84	0.20
HD 60178	HR 2890	9157	5	22	0.99	0.07
HD 60179	HR 2891	9473	4.9	17	0.67	0.07
HD 76644	HR 3569	8242	3.7	138	1.14	0.08	-0.47	0.04	-0.39	0.07
HD 78209	HR 3619	7733	3.5	40	1.05	0.12
HD 79439	HR 3662	8155	4	174	1.04	0.04
HD 80081	HR 3690	8629	4.2	382	-0.28	0.00
HD 85376	HR 3900	7741	3.8	110	1.00	0.03	0.07	0.02	0.36	0.10	-0.65	0.06
HD 87696	HR 3974	8198	4	129	0.98	0.00
HD 89021	HR 4033	9082	4.3	51	0.91	0.14	0.05	0.04
HD 91312	HR 4132	7999	4	119	1.05	0.05
HD 95418	HR 4295	9448	4.3	38	0.70	0.18	-0.18	0.03	-0.39	0.04	-0.50	0.03
HD 95608	HR 4300	9088	4.4	17	0.82	0.16	-0.48	0.08
HD 97603	HR 4357	8428	4.2	178	1.00	0.08
HD 102124	HR 4515	8234	4.1	150	0.90	0.02
HD 102647	HR 4534	8881	4.4	130	1.00	0.13	-0.03	0.03	-0.19	0.06	-0.56	0.04
HD 103287	HR 4554	9308	4.3	168	0.70	0.16
HD 104513	HR 4594	7514	3.5	71	1.11	0.06	0.31	0.01	-0.74	0.05
HD 106591	HR 4660	8860	4.3	370	0.49	0.00
HD 110379	HR 4825	7429	3.7	33	0.90	0.00
HD 110380	HR 4826	7445	3.2	72	1.24	0.06
HD 112412	HR 4914	7184	3.7	32	0.88	0.01
HD 112413	HR 4915	7334	3.1	30.27	-0.29	0.04
HD 116656	HR 5054	8526	3.9	-0.41	0.05
HD 116657	HR 5055	8482	4.2	53	1.18	0.10
HD 125161	HR 5350	7990	3.4	132	1.17	0.06

Table 5
(Continued)

HD	HR	Temperature	log(g)	$v \cdot \sin(i)$	Mg II 4481	\pm error	O I 6158	\pm error	C I 5052	\pm error	C I 7113	\pm error
HD 125162	HR 5351	8883	4.4	120	-1.51	0.15
HD 128167	HR 5447	6931	3.7	15	0.10	0.00
HD 137909	HR 5747	8084	3.9	23	1.75	0.14
HD 139006	HR 5793	9303	4.2	120	0.70	0.15	-0.36	0.00	0.14	0.05
HD 140436	HR 5849	8982	4.6	100	0.50	0.20	-0.08	0.04
HD 141795	HR 5892	8530	3.9	25	0.98	0.07	-0.60	0.03	-0.36	0.07
HD 156164	HR 6410	8673	4	250
HD 159541	HR 6554	7517	3.2	69	0.74	0.06	-0.18	0.03	-0.40	0.07
HD 159560	HR 6555	7488	3.3	47	1.25	0.06
HD 165777	HR 6771	8647	4.3	56	0.87	0.09	0.04	0.03
HD 172167	HR 7001	9296	4.4	15	0.18	0.07	-0.11	0.05
HD 177196	HR 7215	8194	4.1	125	1.05	0.04	-0.32	1.12
HD 180777	HR 7312	7544	4.4	55	1.07	0.02
HD 184006	HR 7420	8385	3.6	250
HD 61421	HR 2943	7008	2.9

Note. The $v \cdot \sin(i)$ here are measured from the Mg 4481 line. The errors in this table represent the measurement error from fitting the models to the data and do not take into account the systematic errors discussed in this paper.

ORCID iDs

Zachary H Draper  <https://orcid.org/0000-0002-1834-3496>
 Brenda Matthews  <https://orcid.org/0000-0003-3017-9577>
 Kim Venn  <https://orcid.org/0000-0003-4134-2042>
 David Lambert  <https://orcid.org/0000-0003-1814-3379>
 Grant Kennedy  <https://orcid.org/0000-0001-6831-7547>
 Tatyana Sitnova  <https://orcid.org/0000-0002-4174-1505>

References

- Alexeeva, S. A., & Mashonkina, L. I. 2015, *MNRAS*, **453**, 1619
 Alexeeva, S. A., Ryabchikova, T. A., & Mashonkina, L. I. 2016, *MNRAS*, **462**, 1123
 Balog, Z., Müller, T., Nielbock, M., et al. 2014, *ExA*, **37**, 129
 Booth, M., Kennedy, G., Sibthorpe, B., et al. 2013, *MNRAS*, **428**, 1263
 Brott, I., & Hauschildt, P. H. 2005, *ESASP*, **576**, 565
 Buchhave, L. A., Bizzarro, M., Latham, D. W., et al. 2014, *Natur*, **509**, 593
 Carter-Bond, J. C., O'Brien, D. P., Delgado Mena, E., et al. 2012, *ApJL*, **747**, L2
 Castellì, F., & Kurucz, R. L. 1994, *A&A*, **281**, 817
 Chen, C. H., Sheehan, P., Watson, D. M., Manoj, P., & Najita, J. R. 2009, *ApJ*, **701**, 1367
 Cutri, R. M., Skrutskie, M. F., van Dyk, S., et al. 2003, *yCat*, **2246**, 0
 De Rosa, R. J., Bulger, J., Patience, J., et al. 2011, *MNRAS*, **415**, 854
 Dekker, H., D'Odorico, S., Kaufer, A., Delabre, B., & Kotzlowski, H. 2000, *Proc. SPIE*, **4008**, 534
 Dommanget, J., & Nys, O. 2002, *yCat*, **1269**
 Draper, Z. H., Matthews, B. C., Kennedy, G. M., et al. 2016, *MNRAS*, **456**, 459
 Fischer, D. A., & Valenti, J. 2005, *ApJ*, **622**, 1102
 Foreman-Mackey, D., Hogg, D. W., Lang, D., & Goodman, J. 2013, *PASP*, **125**, 306
 Gáspár, A., Rieke, G. H., & Ballering, N. 2016, *ApJ*, **826**, 171
 Gebran, M., Monier, R., Royer, F., Lobel, A., & Blomme, R. 2014, in *Putting A Stars into Context: Evolution, Environment, and Related Stars*, ed. G. Mathys et al. (Moscow: Pero), **193**
 Gray, R. O., Riggs, Q. S., Koen, C., et al. 2017, *AJ*, **154**, 31
 Hauck, B., & Mermilliod, M. 1998, *A&AS*, **129**, 431
 Ishihara, D., Onaka, T., Katata, H., et al. 2010, *A&A*, **514**, A1
 Kama, M., Folsom, C. P., & Pinilla, P. 2015, *A&A*, **582**, L10
 Kaufer, A., Stahl, O., Tubbesing, S., et al. 1999, *Msngr*, **95**, 8
 Kennedy, G. M., & Wyatt, M. C. 2014, *MNRAS*, **444**, 3164
 Kennedy, G. M., Wyatt, M. C., Sibthorpe, B., et al. 2012, *MNRAS*, **421**, 2264
 Kubát, J., & Korcáková, D. 2004, in *IAU Symp. 224, The A-Star Puzzle*, ed. J. Zverko et al. (Cambridge: Cambridge Univ. Press), **13**
 Kurucz, R. 1993, *ATLAS9 Stellar Atmosphere Programs and 2 km/s grid Kurucz CD-ROM No. 13* (Cambridge, MA: Smithsonian Astrophysical Observatory), **13**
 Lisse, C. M., Chen, C. H., Wyatt, M. C., et al. 2009, *ApJ*, **701**, 2019
 Maldonado, J., Eiroa, C., Villaver, E., Montesinos, B., & Mora, A. 2012, *A&A*, **541**, A40
 Maldonado, J., Eiroa, C., Villaver, E., Montesinos, B., & Mora, A. 2015, *A&A*, **579**, A20
 Mayor, M., Pepe, F., Queloz, D., et al. 2003, *Msngr*, **114**, 20
 Mermilliod, J. C. 2006, *yCat*, **2122**
 Monnier, J. D., Che, X., Zhao, M., et al. 2012, *ApJL*, **761**, L3
 Moon, T. T., & Dworetzky, M. M. 1985, *MNRAS*, **217**, 305
 Morales, F. Y., Werner, M. W., Bryden, G., et al. 2009, *ApJ*, **699**, 1067
 Murphy, S. J., Corbally, C. J., Gray, R. O., et al. 2015, *PASA*, **32**, e036
 Napiwotzki, R., Schoenberner, D., & Wenske, V. 1993, *A&A*, **268**, 653
 Niedzielski, A., Deka-Szymankiewicz, B., Adamczyk, M., et al. 2016, *A&A*, **585**, A73
 Paunzen, E. 2004, in *IAU Symp. 224, The A-Star Puzzle*, ed. J. Zverko et al. (Cambridge: Cambridge Univ. Press), **443**
 Paunzen, E. 2015, *A&A*, **580**, A23
 Paunzen, E., & Gray, R. O. 1997, *A&AS*, **126**, 407
 Phillips, N. M. 2011, PhD thesis, Institute for Astronomy, The Univ. of Edinburgh
 Phillips, N. M., Greaves, J. S., Dent, W. R. F., et al. 2010, *MNRAS*, **403**, 1089
 Pourbaix, D., Tokovinin, A. A., Batten, A. H., et al. 2004, *A&A*, **424**, 727
 Renson, P., & Manfroid, J. 2009, *A&A*, **498**, 961
 Richer, J., Michaud, G., & Turcotte, S. 2000, *ApJ*, **529**, 338
 Rodriguez, D. R., Duchêne, G., Tom, H., et al. 2015, *MNRAS*, **449**, 3160
 Sbordone, L., Bonifacio, P., Castellì, F., & Kurucz, R. L. 2004, *MSAIS*, **5**, 93
 Sitnova, T. M., Mashonkina, L. I., & Ryabchikova, T. A. 2013, *AsTL*, **39**, 126
 Skumanich, A. 1972, *ApJ*, **171**, 565
 Sneden, C. A. 1973, PhD thesis, The Univ. of Texas at Austin
 Sousa, S. G., Santos, N. C., Israelian, G., Mayor, M., & Monteiro, M. J. P. F. G. 2007, *A&A*, **469**, 783
 Su, K. Y. L., Rieke, G. H., Stansberry, J. A., et al. 2006, *ApJ*, **653**, 675
 Takeda, Y. 1997, *PASJ*, **49**, 471
 Takeda, Y., Han, I., Kang, D.-I., Lee, B.-C., & Kim, K.-M. 2008a, *JKAS*, **41**, 83
 Takeda, Y., Kawanomoto, S., & Ohishi, N. 2007, *PASJ*, **59**, 245
 Takeda, Y., Kawanomoto, S., & Ohishi, N. 2008b, *ApJ*, **678**, 446
 Thureau, N. D., Greaves, J. S., Matthews, B. C., et al. 2014, *MNRAS*, **445**, 2558
 Tull, R. G., MacQueen, P. J., Sneden, C., & Lambert, D. L. 1995, *PASP*, **107**, 251
 Turcotte, S. 2002, *ApJL*, **573**, L129
 Venn, K. A., & Lambert, D. L. 1990, *ApJ*, **363**, 234
 Vican, L. 2012, *AJ*, **143**, 135
 Wedemeyer, S. 2001, *A&A*, **373**, 998
 Wright, E. L., Eisenhardt, P. R. M., Mainzer, A. K., et al. 2010, *AJ*, **140**, 1868
 Wyatt, M. C. 2008, *ARA&A*, **46**, 339
 Yoon, J., Peterson, D. M., Kurucz, R. L., & Zagarellò, R. J. 2010, *ApJ*, **708**, 71
 Yoon, J., Peterson, D. M., Zagarellò, R. J., Armstrong, J. T., & Pauls, T. 2008, *ApJ*, **681**, 570
 Zhao, J.-K., Zhao, G., Chen, Y.-Q., et al. 2006, *CJAA*, **6**, 689
 Zhu, W., Wang, J., & Huang, C. 2016, *ApJ*, **832**, 196
 Zięliński, P., Niedzielski, A., Wolszczan, A., Adamów, M., & Nowak, G. 2012, *A&A*, **547**, A91